JACS
JOURNAL OF THE AMERICAN CHEMICAL SOCIETY

Article

pubs.acs.org/JACS

Direct Measurement of Adsorbed Gas Redistribution in Metal–Organic Frameworks

Ying-Pin Chen,[†,‡] Yangyang Liu,[‡] Dahuan Liu,[‡,§] Mathieu Bosch,[‡] and Hong-Cai Zhou*[,†,‡]

[†]Department of Materials Science and Engineering, and [‡]Department of Chemistry, Texas A&M University, College Station, Texas 77843, United States

[§]State Key Laboratory of Organic–Inorganic Composites, Beijing University of Chemical Technology, Beijing 100029, China

Supporting Information

ABSTRACT: Knowledge about the interactions between gas molecules and adsorption sites is essential to customize metal-organic frameworks (MOFs) as adsorbents. The dynamic interactions occurring during adsorption/desorption working cycles with several states are especially complicated. Even so, the gas dynamics based upon experimental observations and the distribution of guest molecules under various conditions in MOFs have not been extensively studied yet. In this work, a direct time-resolved diffraction structure envelope (TRDSE) method using sequential measurements by in situ synchrotron powder X-ray diffraction has been developed to monitor several gas dynamic processes taking place in MOFs: infusion, desorption, and gas redistribution upon temperature change. The electron density maps indicate that gas molecules prefer to redistribute over heterogeneous types of sites rather than to exclusively occupy the primary binding sites. We found that the gas molecules are entropically driven from open metal sites to larger neighboring spaces during the gas infusion period, matching the localized-to-mobile mechanism. In addition, the partitioning ratio of molecules adsorbed at each site varies with different temperatures, as opposed to an invariant distribution mode. Equally important, the gas adsorption in MOFs is intensely influenced by the gas–gas interactions, which might induce more molecules to be accommodated in an orderly compact arrangement. This sequential TRDSE method is generally applicable to most crystalline adsorbents, yielding information on distribution ratios of adsorbates at each type of site.

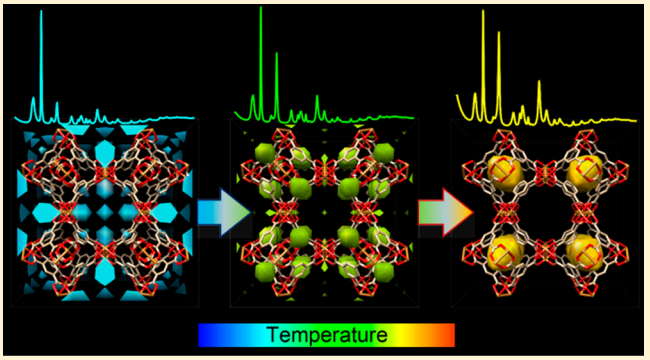

INTRODUCTION

Metal–organic frameworks (MOFs), a family of advanced porous materials, have been considered a promising candidate for CO_2 capture and CH_4 storage.[1] Superior in porosity and customizability to the conventional zeolite materials, desired architectures of MOFs can be easily tailored by elegant choice of metal clusters and organic linkers.[2] Accordingly, perceiving which structural characteristics contribute to high gas uptake is of critical importance in the design of materials with better adsorption capacity.[3] There have been several endeavors to develop this fundamental knowledge: density functional theory (DFT),[4] molecular simulations,[5] and powder neutron diffraction experiments.[5a,6,7] Unfortunately, some discrepancies were found among these reports, arising from different methods or force fields adopted in computational simulations. On the other hand, neutron diffraction successfully identified the precise adsorption sites in several classical MOFs, yet most diffraction experiments were done below CH_4 condensation temperatures (111 K),[6a−c] which might not reflect real gas behaviors under practical conditions.

Granted that some mechanisms are proposed accurately in certain MOF systems, in practice, MOFs do not simply sit in these static and monotonous situations.[8] MOFs can be potentially used under a wide range of environments, such as in the flues of power plants and cold chambers of NGV cylinder tanks (natural gas vehicle).[1b] Even a specific system might undergo several state shifts in one working cycle so it is possible that structural features can be beneficial for one stage but harmful in another stage. Moreover, MOF regeneration requires a process of pressure and/or temperature change to desorb gases. How the gas kinetic behaviors facilitate a fast and complete thermodynamic equilibrium of adsorption/desorption remains an unexplored field, even though understanding gas dynamics in MOFs may allow significantly more effective design.[8]

In an attempt to overcome the drawbacks of the investigation methods mentioned above, chronological differential electron density (DED) maps were three-dimensionally visualized for the positional evolution of guest molecules under reasonable ambient conditions. This structure envelope concept has been applied in identifying the guest molecules in crystalline adsorbents,[9] distinguishing the positively and negatively charged ions,[10] separating interpenetrated MOF networks,[11]

Received: October 8, 2014
Published: February 12, 2015

DOI: 10.1021/ja5103579
J. Am. Chem. Soc. 2015, 137, 2919–2930

and detecting diffusion of indicator molecules.[12] In this Article, we particularly focused on elucidating the time- and temperature-dependence of gas dynamics in MOFs. Synchrotron-based X-ray measurements were necessarily employed due to the insufficient resolution of regular diffractometers. For this time-resolved diffraction structure envelope (TRDSE) method, we took sequential X-ray exposures on a crystal under specific gas atmospheres, recording a series of powder patterns as a function of gas-loading time and temperatures. It can be seen that the intensity of certain (*hkl*) reflections was increased or decreased due to electron scattering from these gas molecules adsorbed on the corresponding (*hkl*) planes. Intersections of several (*hkl*) planes are correlated to structural features in the unit cell of MOFs; hence, the preeminent adsorption sites were identified. Combining this with an adequate statistical cutoff level for the series of DED maps, different maps are objectively compared.

Four gas dynamic processes were successfully observed via DED interpretation (Figure 1), which is the first example of experimental crystallographic measurement of gas migration. Additionally, we explore a general consequence of thermodynamics for the gas dynamics in MOFs. These measurements reveal how the guest molecules conduct the redistribution over the host framework surfaces to reach the minimum of free energy. Our studies also show that the open metal sites and the window openings emphasized in earlier efforts are not always so crucial.[4a,b,6b,c] The entropic driving force, appropriate accessibility, and the gas−gas interactions might be as or more important than the binding sites with unscreened Coulomb force or van der Waals force under certain conditions.

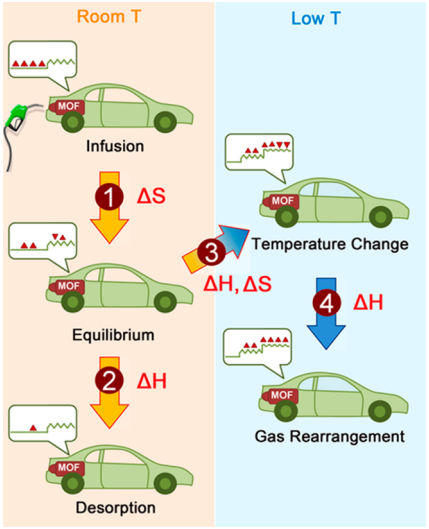

Figure 1. Four CH_4 dynamic processes taking place in MOFs were observed in our work: (1) kinetic transition during the gas infusion period, (2) desorption residues, (3) molecular redistribution upon temperature change, and (4) gas−gas interactions at low temperature. Process 1 is entropically driven, while processes 2 and 4 are enthalpically driven. The molecular distribution over various energetic sites on MOF surfaces is depicted in the dialogue boxes, which will be explained below. The orientations of the triangles conceptually denote the orientations of gas molecular arrangements. Similar work about CO_2 behavior can be found in Supporting Information section 4.

METHODOLOGY

Differential electron density (DED) maps are 3-D iso-surfaces, which are constructed of the differences between two structure envelopes. Building a structure envelope is a procedure to describe crystal structures with hyperbolic surfaces.[10−13] These surfaces can be mathematically expressed by a Fourier summation with structure factor phases φ_{hkl} and the normalized structure factor amplitudes $|E_{hkl}|$ of a few selected reflections (*hkl*), which are given by[14]

$$\rho(x, y, z) = \sum_{hkl} |E_{hkl}| \cos(2\pi(hx + ky + lz) - \varphi_{hkl}) \quad (1)$$

where $\rho(x,y,z)$ denotes the electron density distribution of the structure envelope. Structure envelopes also divide a unit cell into areas of rich and deficient electron density. In the MOF field, this contrast surface characterizes the framework atoms as appearing on the positive side and the pore spaces on the negative side.[15] Furthermore, envelope surfaces assembled by Fourier series are derived as fundamental invariants of structured matter.[11,14] This means that if the crystallographic symmetry and unit cell parameters remain unchanged, the sheathing envelope will still be similar.

Accordingly, an observed porous crystal filled with various gas molecules should have an envelope analogous to its reference model. The difference between these two envelopes (ρ_{obs} and ρ_{ref}) comes from the electron scattering of gas molecules, which is written as[9]

$$\rho_{gst} = \rho_{obs} - k\rho_{ref} \quad (2)$$

where *k* is the scaling factor defined as the quotient of maximum values of ρ_{obs} and ρ_{ref}. The contouring of ρ_{gst}, according to the DED map, will constitute a 3-D distribution in the unit cell, visualizing the position of the guest molecules.

In this work, the electron scattering of gas molecules in all examples is only responsible for the amplitude changes of certain reflections, not for phase switching. Note that the TRDSE method is only valid when there is a negligible breathing effect[16] or phase transition in the framework on gas adsorption. Therefore, the structure factor phase will be fixed for both ρ_{obs} and ρ_{ref}, while the structure factor amplitudes will be replaced with $|E_{hkl}^{ref}|$ for ρ_{ref} and $|E_{hkl}^{obs}|$ for ρ_{obs}. The operational details will be described in the next section.

EXPERIMENTAL SECTION

A. MOF Synthesis and Activation. Four MOF compounds, HKUST-1,[17] PCN-12,[18] and PCN-306/307,[19] were chosen as representatives for their exceptional CH_4 uptake and diverse structural features of interest, such as open Cu(II) sites, window pockets, cage corners, and empty cages (Figure 2). All compounds were crystallized according to the original procedures, followed by solvent exchange with methanol and dichloromethane, and then vacuumed at 150 °C for

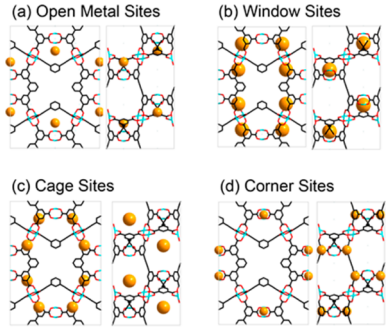

Figure 2. Common structural features in MOFs: (a−d) Definition of four adsorption sites for PCN-306, viewed along the *c*-axis (left) and *a*-axis (right). The copper, oxygen, and carbon atoms are cyan, red, and black, respectively. The hydrogen atoms are omitted for clarity. The definition for HKUST-1 is given in Supporting Information Table S3.1.

DOI: 10.1021/ja5103579
J. Am. Chem. Soc. 2015, 137, 2919−2930

10 h. These Cu-MOFs changed from blue to purple, exhibiting successful solvent removal from the Cu_2 units. The activated crystals were preserved in dichloromethane before diffraction experiments.

B. Experimental Setup and Data Collection. In situ synchrotron-based powder diffraction experiments were performed at the 17-BM beamline of the Advance Photon Source in Argonne National Laboratory. The incident beam wavelength was 0.72959 Å for HKUST-1, 0.72808 Å for PCN-12, and 0.72910 Å for PCN-306/307, respectively. The ground powdery samples were packed in a polyimide capillary, installed on a flow-cell,[20] and then activated at 423 K for an hour to evacuate coordinated water molecules. An intensity-2θ pattern was collected at 295, 200, and 150 K under an atmosphere of He (as reference and flush), CO_2, and CH_4. In each gas loading period, patterns were recorded by sequential exposures at an interval of 30 s taking 10−20 min to obtain data for a dynamic process (Figure 3a).

C. Amplitude Extraction. According to eq 1, the normalized structure factor amplitudes $|E_{hkl}|$ and the structure factor phases φ_{hkl} are the two sets of data needed to construct the DED maps. The intensity amplitude of measured PXRD patterns was extracted by Le Bail refinement built in to the JANA2006 software.[21] The refinement steps were described as follows. Data recorded at 2θ smaller than 2° and larger than 16° were ignored.[22] The pattern backgrounds were modeled with 20-term Legendre polynomials, and the zero shift term was corrected for experiments performed in transmission geometry (Debye−Scherrer form). The refinement of unit cell parameters was initially started from the axial length of the single crystal proposed in the original publications.[17−19] The peak profiles were fitted with the pseudo-Voigt function[23] (details in Supporting Information section 1.2).

The agreement of Le Bail fittings with the measured data was evaluated by the residuals in final whole pattern decomposition plots (Figure 3b), and by the *R*-factors shown in Supporting Information Table S3.2. It can be seen that the final unit cell parameters do not shift noticeably, denoting no phase transition or material deterioration in the crystal. This is a prerequisite for the systems, which can be analyzed with the TRDSE method.

D. Reflection Selection and Phase Determination. Taking HKUST-1 ($Fm\bar{3}m$) as an example, eight reflections, (111), (002), (202), (113), (222), (004), (313), and (224), were chosen for fitting surface generation in all gas-loaded crystals (Supporting Information Table S3.3). For PCN-30X and PCN-12, 12 and 11 reflections were selected as shown in Supporting Information Table S3.6/10/12.

The "threshold resolution" has to be calculated as the selection criteria. For example, if the narrowest part of the structure is 5.7 Å (the width of the window openings), the threshold will be 2θ of 7.3° that the reflection selection has to go beyond. Note that these reflections (*hkl*) have to be selected such that all directions in reciprocal space are represented and that their indices should be lower to avoid serious peak overlap[13,24] (details in Supporting Information sections 1.3 and 1.6).

This set of reflections needs to be checked for structure factor phase changes during the investigated process. If the phases are switching, the intensity of that peak will go to zero. In all four cases, no reflections disappeared in the PXRD patterns (Supporting Information Figure S3.2/9/13/15), suggesting the corresponding phases remain the same. The phases were obtained from known MOF structures, for which ideal structure factor phases, φ_{hkl}^{calc}, were calculated (Supporting Information section 1.4).[15]

As a reliability inspection, it is necessary to overlap the generated envelope with the known crystal model[15] to confirm that no other unreasonable experimental artifacts are introduced.

E. Difference of Electron Density. The resulting electron density maps were reconstructed on unit cell grids using the inverse discrete Fourier transform in the SUPERFLIP program.[25] An INFLIP setup file for SUPERFLIP was initialized by assigning the selected reflection set containing ideal phases and the extracted squared amplitudes (format in Supporting Information section 1.5). After the algorithm, a 3-D matrix in XPLOR format representing the electron density, $\rho(x,y,z)$, at each grid point in real space was generated. The subtraction of two density maps ($\rho_{obs} - k\rho_{ref}$) and the visualization of the density

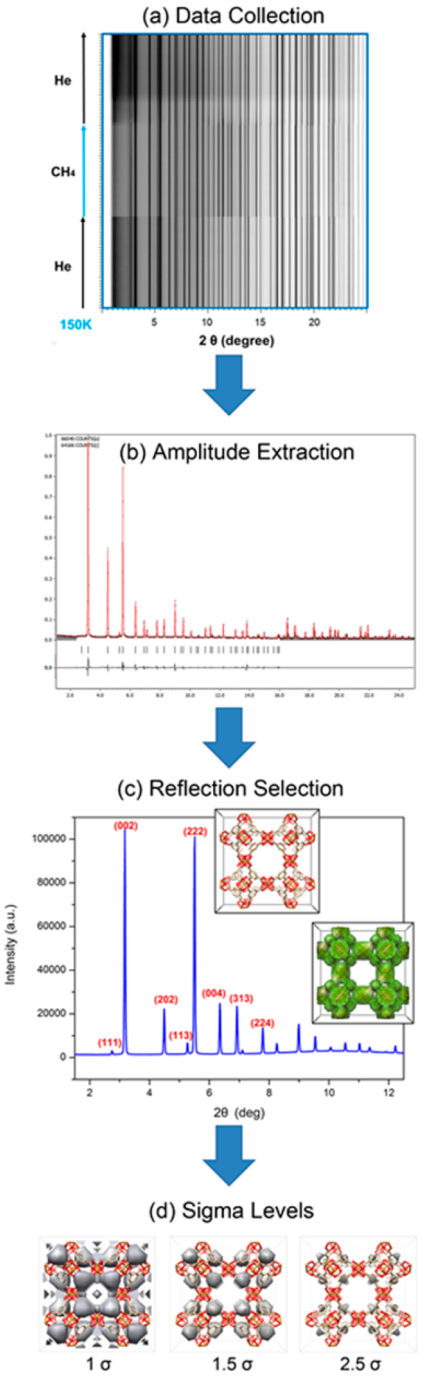

Figure 3. Algorithm for the TRDSE method. (a) Top view of the in situ synchrotron-based powder diffraction; (b) Le Bail refinement to extract the intensity amplitudes; (c) structure envelope generation using selected reflections; and (d) different σ levels to describe the DED maps.

difference (ρ_{gst}) can be made using UCSF Chimera software.[26] The absolute value of ρ_{gst} in the unit of "electrons per Å^3" can be obtained by scaling with the electron density of the framework.[27]

F. Contour Plots, σ Levels, and Validity Tests. To track down the gas adsorption sites by mapping the evolution of the electron density, a consistent cutoff point for contouring different density maps with varied measuring conditions was required. There is a statistical description for the $\rho(x,y,z)$ distribution to solve this problem: the mean and the standard deviation (σ) of $\rho(x,y,z)$ across the entire mapping space. The relative density of every grid point presented in $\rho(x,y,z)$ can be represented in σ units away from the mean.[28] An

DOI: 10.1021/ja5103579
J. Am. Chem. Soc. 2015, 137, 2919−2930

appropriate contour level was anticipated to find the absent matter or missing fragments from the reference model. In this case, the fragments represent CH_4 or CO_2 molecules. For the system of HKUST-1 and PCN-306/307, the cutoff level of DED maps (ρ_{gst}) was contoured around 1.5σ above zero (Figure 3d); for PCN-12, it was 1.7σ.

Note that the termination errors usually occur on a center of inversion, presenting spurious peaks in the pore environments. The DED maps should be carefully examined to see if strong peaks shown in pores come from the termination errors. The benchmarking procedure not only provides a way to evaluate the validity of the DED maps, but eliminates the spurious peaks in the pores as well.[9]

G. Error Sources and Potential Problems. DED mapping might be meaningless without considering two major error sources.[9] One is the Fourier truncation error caused by the limited number of the selected reflections. This error can be decreased by using a greater number of reflections. However, selecting those reflections within the threshold angle is sufficient to construct a well-fitting envelope with an acceptable error (Supporting Information section 1.6). Another source of error is the structural transformations caused by the temperature/pressure/atmosphere changes during the measurements. In this work, the empty MOFs (in He atmosphere) at various temperatures were adopted to be the reference envelope (ρ_{ref}), which is helpful to minimize this second error.

On the other hand, inhomogeneous sampling might cause a potential problem in the experiment processes. In our experimental setup, a 0.3 mm round X-ray beam through the center of a capillary with 0.8 mm inner diameter covers over 45% of the cross section area (Supporting Information Figure S1.4). The measurement averages the diffraction from thousands of microcrystallites, and the study on the gas redistribution events is no exception. Apart from the problem with sample inhomogeneity, many states of order/disorder and transport in the material might be sampled simultaneously, resulting in peak width broadening. The $F^2(hkl)$ difference integrated from the profile function, instead of the intensity maximum difference, can take the peak width change into account in the calculation. In this work, we can see that the peak widths in the in situ PXRD patterns (Supporting Information Figure S3.2/9/13/15) barely change after gas loading at room temperature, suggesting the state change is trivial. Although the peak width changes at low temperatures, using the maximum difference is sufficient to obtain gas distribution profiles because the change usually happens at the low intensity reflections. Other inhomogeneity problems caused by thermal gradients were described in Supporting Information section 1.7.

RESULTS AND DISCUSSION

Experimental DED Mapping Results As Compared to Literature and Simulation. Past research has shown that gas molecules are located at up to eight distinct sites in MOF-5 and HKUST-1.[3,7d] For CH_4 storage in HKUST-1, the open Cu(II) sites and the window openings were proposed to be the primary adsorption sites, while the center of the small octahedral cages and the corner of large cuboctahedral cages were the secondary adsorption sites.[5a] In our DED maps (Figure 4, right), strong electron density is located in the small octahedral cages at 295 K, at the window openings at 200 K, and around the large cage corners at 150 K, respectively. This is also found in the ensemble-averaged maps predicted by the Monte Carlo simulation in Materials Studio[29] (Figure 4, left).

These consistent outcomes were also recognized in the noble gas system, where the gas molecules could be considered CH_4-like particles.[6d] Both the published literature and our simulations confirm the validity of the TRDSE method. It is worth mentioning that the open metal sites show adsorption of CO_2 molecules at room temperature (Supporting Information section 4). In the following sections, four gas dynamic processes are graphically demonstrated. Infusion and desorption as well as temperature evolution and gas rearrangement are elucidated by the chronological DED maps, and possible enthalpic and entropic rationalizations are discussed. Finally, a comprehensive examination describes the minute differences between a pair of analogues, PCN-306 and PCN-307. All of the maps in this article were shown in yellow for the samples measured at 295 K, green for 200 K, and blue for 150 K. Different perspectives of the four MOF structures and the corresponding DED maps were drawn in the Supporting Information for clarity.

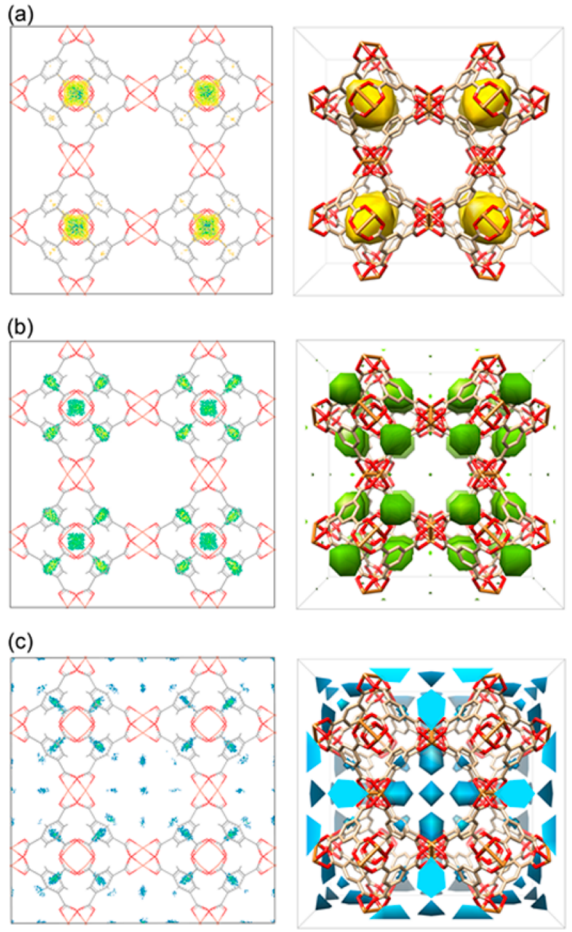

Figure 4. Agreement between the computational (left) and experimental (right) results of CH_4 adsorption at (a) 295 K, (b) 200 K, and (c) 150 K in HKUST-1.

1. Initial Adsorption in MOFs. Gas infusion into MOFs is the most common process in all gas-related applications. However, the gas kinetics in the initial CH_4 adsorption are still unclear. To capture the instantaneous changes at the early stage, the gas flow rate should be as slow as possible. Herein, the CH_4 flow rate was regulated as approximately 0.4 mm^3/s. The studied objects, PCN-30X and PCN-12, have 3-fold window openings, which will be the focus in this section.

Interpreted from the differences between the reference and the CH_4-loaded crystals, a molecular transport path was observed between the coordinately unsaturated metal units and the window sites. In Figure 5 measured at 295 K, the CH_4 molecules approached the open Cu sites along the *c*-axis at the very beginning (Figure 5a), followed by the increasing CH_4 population at the open Cu sites and in the window pockets (Figure 5b). Successively, the major portion of CH_4 molecules migrated[30] from the open Cu sites to the window pockets

DOI: 10.1021/ja5103579
J. Am. Chem. Soc. 2015, 137, 2919−2930

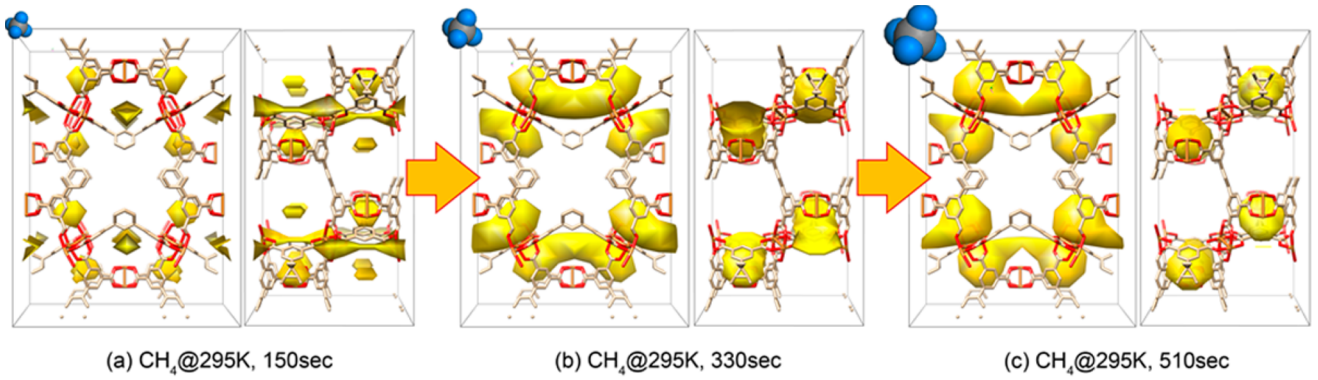

Figure 5. DED snapshots illustrate the kinetic transition in the CH_4 adsorption process in PCN-306. The perspectives are viewed along the *c*-axis (left) and *a*-axis (right). The CH_4 flow was introduced into the crystals, followed by sequential X-ray measurements after (a) 150 s, (b) 330 s, and (c) 510 s, under controlled conditions of 295 K and 1 bar. Yellow clouds represent the most significant adsorption regions with contouring at 1.5σ.

Table 1. Summary of the Time-Dependent PXRD Experiments Performed on PCN-306 and PCN-12, Including the Measurement Conditions, the Gas Loading Times, the Absolute Values of the Contour Levels, the Total Volumes and Surfaces of the Electron Clouds Regions Shown in Figures 5 and 6, and the Relative Ratios of Electron Quantity[a]

compound	conditions	time (s)	contour level	volume (Å^3)	surface (Å^2)	surf/vol	electron ratio
PCN-306	295 K, 1 bar	150	0.00146	380.9	1005.2	2.6	0.56
		330	0.00372	1154.0	1219.4	1.1	4.29
		510	0.00390	817.6	920.7	1.1	3.18
	150 K, 1 bar	120	0.000735	196.7	777.2	4.0	0.14
		300	0.0110	571.2	754.8	1.3	6.28
		540	0.0158	753.2	1075.0	1.4	11.90
PCN-12	295 K, 1 bar	30	0.00173	361.8	768.3	2.1	0.63
		150	0.00206	362.3	677.3	1.9	0.75
		630	0.00282	1221.0	1071.0	0.9	3.44

[a]The contour level is 1.5σ for PCN-306 and 1.7σ for PCN-12.

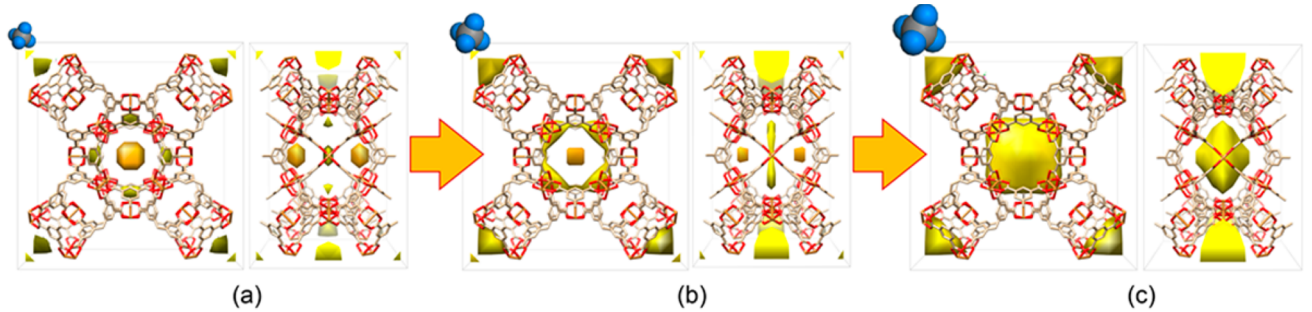

Figure 6. DED snapshots illustrate the kinetic transition of the CH_4 adsorption process in PCN-12. These are viewed along the *c*-axis (left) and *a*/*b*-axis (right). The CH_4 flow was introduced into the crystals, followed by sequential X-ray measurements after (a) 30 s, (b) 150 s, and (c) 630 s, at 295 K and 1 bar.

(Figure 5c), completing a "kinetic transition". This indicates that the open metal sites perform as kinetic first attractors that direct CH_4 molecules to thermodynamically stable adopters.[31] Also, the first docked molecule is a directing agent of subsequent molecules, as it facilitates the sorption to spread throughout the whole structure starting from the open metal sites.[32]

This phenomenon of kinetic transition did not occur only at room temperature; it also happened near the condensation temperature of CH_4 (Supporting Information section 3.2.5). At 150 K, a small amount of CH_4 molecules were attracted to the open Cu sites at the onset. In seconds, the incoming CH_4 molecules navigated to the adjacent cages (Figure 2c) rather than moving into the window pockets, reaching another thermodynamically favored site. With continuous CH_4 addition, the large pores were gradually filled along the *a*-axis of the crystal (Figure 11c). The temperature effect on the final states of gas migration will be discussed in the section describing gas redistribution with temperature change. Although the CH_4 destinations at the two temperatures (295/150 K) were different, both of the surface/volume ratios of the observed CH_4 electron clouds decreased with loading time (Table 1). This displays a visible tendency of surface minimization upon CH_4 infusion. The parallel results of PCN-307 can be found in Supporting Information section 3.3.5. To the best of our knowledge, this is the first example of experimental evidence of the kinetic transition of gas molecules in MOFs.

To deeply study the kinetic transition from open Cu sites to other structural spaces, further analysis was done on PCN-12.

DOI: 10.1021/ja5103579
J. Am. Chem. Soc. 2015, 137, 2919−2930

In addition to the 3-fold window sites (Figure 7c), PCN-12 is also constructed by larger 4-fold openings (Figure 7b), and there are various sizes of cages in the structure. As shown in Figure 7a, PCN-12 comprises four Wyckoff positions of Cu_2 units. As viewed along the *c*-axis, the Cu_2 units labeled with 8*s*/4*k* as well as those with 8*r*/4*o* build identical symmetrical cages 11 Å wide. The 8*s*/4*o* units form large ellipsoidal cages 17 Å long, and the 8*r*/4*k* units form small cavities 9 Å wide. The cages constructed by different sets of open metal sites were not equivalently accessible for CH_4 molecules. The cages consisting of 8*r*/4*o* sets and 8*s*/4*k* sets were populated with CH_4, whereas those with the 8*s*/4*o* and 8*r*/4*k* sets were left vacant. This nonequivalence of CH_4 amounts on these open metal sites indicates that gas molecules discriminate among the binding sites in favor of those with nearby multipoint interactions[4c] and appropriate spatial accessibility.

Another kinetic transition occurred on this adsorbent. In Figure 6a, the CH_4 molecules were trapped by the open Cu sites 4*o* and the 4-fold window openings, both of which are the most easily accessible regions on the central channels. In Figure 6b, the transition direction changed from the open Cu sites (Wyckoff 4*o*) to the larger 4-fold window openings but not the smaller 3-fold sites. The DED contours showed a close ring connecting the area between the open Cu sites and their bordering 4-fold window openings. Further CH_4 loading did not diffuse homogeneously into the small volume, which contains the available open Cu sites classified as 4*k*. Instead, CH_4 molecules aggregated in the center of the channels to reach the surface minimum (Figure 6c and Table 1).

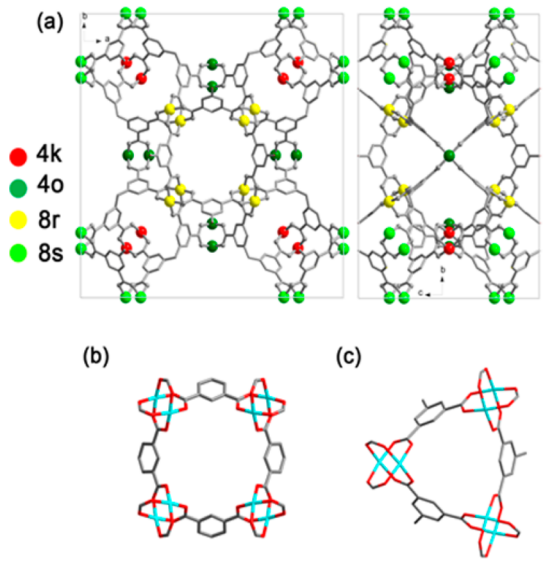

Figure 7. (a) Wyckoff positions labeled for Cu_2 units in PCN-12, viewed along the *c*-axis (left) and *a*/*b*-axis (right). PCN-12 comprises (b) 4-fold window openings (four pairs of Cu_2 units and phenyl rings) and (c) 3-fold window openings.

Consequently, this time-dependent kinetic transition can be recognized at various temperatures and in different adsorbents. Especially for Figure 5b,c,[33] the transition continues at the near equilibrium state. We attribute this unusual behavior, molecular transport from one binding site to another, to an inevitable consequence of thermodynamics. On the basis of the basic thermodynamic relationship:

$$\Delta G = \Delta H - T\Delta S \tag{3}$$

the transition process will be spontaneous ($\Delta G < 0$) if one of the following conditions is true: (a) $\Delta H < 0$, $\Delta S > 0$, (b) $\Delta H < 0$, $\Delta S < 0$, plus $|T\Delta S| < |\Delta H|$, or (c) $\Delta H > 0$, $\Delta S > 0$, plus $|T\Delta S| > |\Delta H|$, where $\Delta H < 0$ is defined as exothermic heat, and $\Delta S < 0$ refers to the transition to fewer molecular degrees of freedom in the process. According to Wu et al.'s report,[5a] the CH_4 binding energy of open metal sites is around 25 kJ/mol, roughly identical to that of window sites.[34] This means that $|\Delta H|$ is extremely small. We attribute this discovery to (c); that is, the gas molecules will be able to break away from the potential well if $T\Delta S \geq \Delta H \approx 0$. More precisely, we made an effort to investigate how this entropic driving force pushes gas molecules out of the potential well in the equilibrium states. A localized-to-mobile model,[35] considering the adsorbates partially localized and partially mobile, was hypothesized to fit our observations.

In this model simplified with statistical treatment[35a] (details in Supporting Information section 5), f is introduced to define the maximum fraction of the adsorbent surfaces on which adsorbates can be localized. θ_l and θ_m are the fractions of truly adsorbed molecules on the localized and mobile areas, respectively. N_{sl}, N_l, and N_m are the molecular numbers corresponding to f, θ_l, and θ_m. The relationship between the above parameters can be expressed as

$$f = N_{sl}/N_s,\ \theta_m = N_m/N_s,\ \theta_l = N_l/N_s,\ \theta = \theta_l + \theta_m$$

where N_s is the maximum number of the molecules that can be adsorbed on all solid surfaces. The partition functions for a localized molecule (q_l) and for a mobile molecule (q_m) are

$$q_l = q_{vx}q_{vy}q_{vz}\exp\left(-\frac{u_{pl}}{kT}\right) \tag{4}$$

$$q_m = \left(\frac{2\pi mkT}{h^2}\right)q_{vz}a_s\exp\left(-\frac{u_{pm}}{kT}\right)[N_s(1-f) - N_m] \tag{5}$$

where u_{pm} and u_{pl} are the corresponding potential energy in adsorbed states. q_{vx}, q_{vy}, and q_{vz} are the vibrational partition functions in x, y, and z directions. $(2\pi mkT/h^2)$ is the translational partition function. q'_m is the partition function for mobile molecules without size correction, which is given as $q'_m = (2\pi mkT/h^2)q_{vz}a_s\exp(-(u_{pm}/kT))$.

The molecular distribution over mobile and localized regions can be derived as:[35a]

$$\frac{\theta_m}{(1-f-\theta_m)q'_m}\exp\left(\frac{\theta_m}{1-f-\theta_m}\right) = \frac{\theta_l}{(f-\theta_l)q_l} \tag{6}$$

To present eq 6 in a figure, the relative value of q'_m and q_l and possible f have to be estimated from eqs 4 and 5. A CH_4 molecule has a mass (m) of 2.66×10^{-26} kg and a cross-sectional area[36] (a_s) of 0.164 nm^2. For simplicity, all vibrational partition functions were assumed to be unity and $u_{pm} = u_{pl}$. Substituting into eqs 4 and 5, $(q'_m/q_l) = 254$ was obtained. The distributive ratios of the localized CH_4 (θ_l/θ) were graphically depicted with an assumption of $(q'_m/q_l) = 10$, 30, 100, and 254 in Figure 8a, and $f = 0.3$, 0.5, 0.7, and 0.9 in Figure 8b, respectively. All of the curves possess a maximum before full coverage ($\theta = 1.0$).

We selected $(q'_m/q_l) = 30$ and $f = 0.5$ as representative (blue trace in Figure 8c). It is expected that (θ_l/θ) approaches f with a positive slope; nevertheless, an interesting range showing $(\theta_l/\theta) > f$ occurs at near 85% of the coverage ($\theta \approx 0.85$), and thus a negative slope is necessary to complete full coverage. One of

DOI: 10.1021/ja5103579
J. Am. Chem. Soc. 2015, 137, 2919−2930

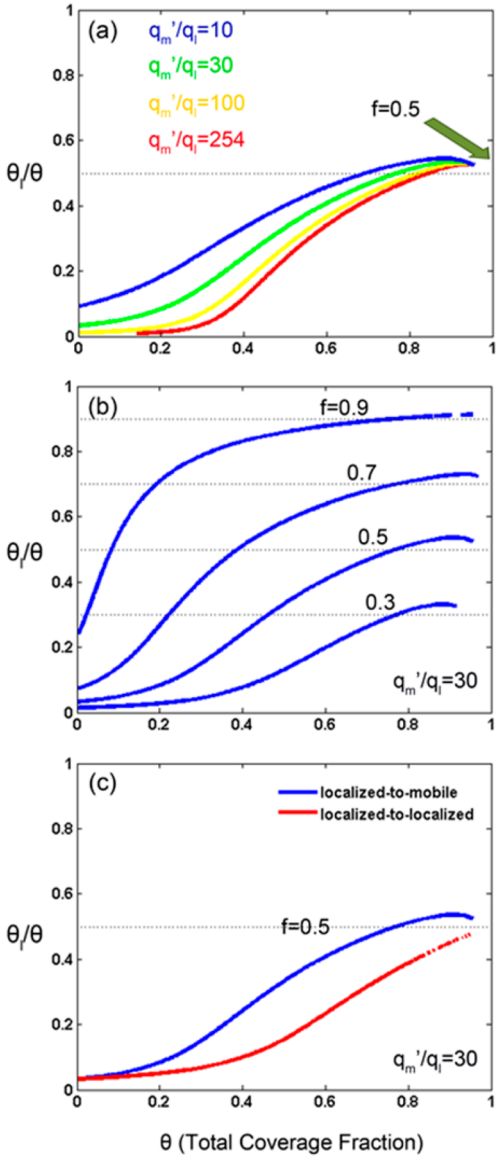

Figure 8. Molecular distribution over localized regions on heterogeneous surfaces (the graphical presentation of eq 6). The fraction of the localized adsorbates on the adsorbent surface if (a) the ratio of (q'_m/q_l) varies, or (b) the maximum fraction of localized adsorbates, f, varies. (c) Theoretical derivation for localized-to-mobile case and localized-to-localized case.

the possibilities for the negative slope of $((\Delta\theta_l/\theta)/\Delta\theta)$ is molecular transport from a localized area to a mobile area. If the open metal sites and the nearby window pockets are regarded as a localized part and a mobile part for adsorbates, respectively, the localized-to-mobile model will match our experimental observations of kinetic transition in PCN-30X and PCN-12. However, if both the open metal sites and the window sites are localized parts, the exponential term in eq 6 will be absent, resulting in a monotonic increasing function without any negative slopes in Figure 8c (red trace). That also means no molecular transport will happen under the localized-to-localized assumption.

In summary, the sequential measurements of in situ powder X-ray diffraction give insight into gas kinetic transitions occurring between open metal sites and the neighboring structural spaces. Despite the fact that the open metal sites possess potential wells and significant exothermic enthalpy, there is another possibility to reach minimum Gibbs energy for the adsorption process by increasing entropy. In this section, we experimentally visualized the abstract concept of this entropy-driven process. The localized-to-mobile mechanism was proposed for the cause of gas kinetic transition, supporting the observations of molecular transport from one site to another.

2. Desorption in MOFs. Engines running on CH_4 require an exhaust pressure to operate. The usable working capacity and the regeneration efficiency are as important as the gas uptake performance.[34] In other words, the speed and completeness of desorption is another key indicator to evaluate the industrial applicability of a MOF material for methane storage.

As a result, in Figure 9a and c, the CH_4 molecules sit in the small octahedral cages, whereas CO_2 molecules primarily[37] lie

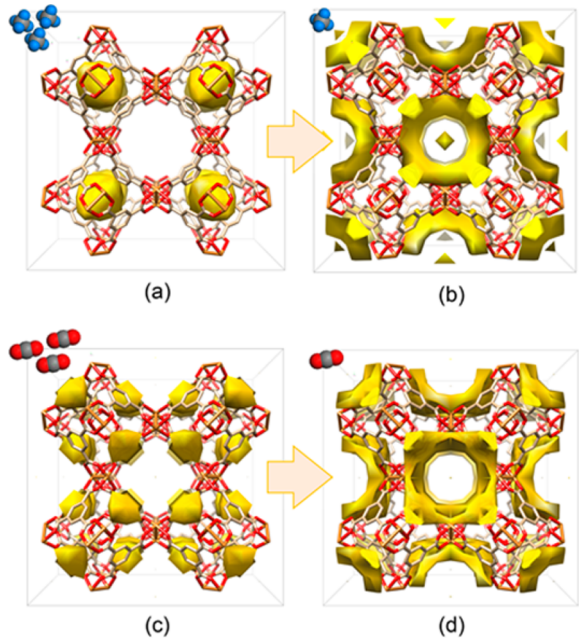

Figure 9. DED snapshots illustrate the evolution of CH_4/CO_2 desorption in HKUST-1 at 295 K. The experiment procedure was controlled as follows: (a) CH_4 loading for 1500 s, (b) followed by He flushing for 300 s; and (c) CO_2 loading for 1500 s, (d) followed by He flushing for 300 s.

on the window openings in the adsorption states. As opposed to the distinctive features for CH_4 and CO_2 adsorption, the maps for these two desorption processes become consistent. Both of the gas residues were detected around the open metal sites (Figure 9b,d, Table 2), exhibiting the final desorbed molecules being stuck around the sites possessing strong electrostatic force.

Table 2. Ratios of Relative Electron Quantity Detected in the Four States Corresponding to Figure 9

gas	state	electron ratio
CH_4	(a) adsorption	12.2
	(b) desorption	2.7
CO_2	(c) adsorption	11.7
	(d) desorption	3.5

DOI: 10.1021/ja5103579
J. Am. Chem. Soc. 2015, 137, 2919−2930

According to our work on initial adsorption, the open metal site is the first attractor. Additionally, the open metal site is also the last area of significant gas molecule presence in desorption. A site possessing higher adsorption enthalpy will be more attractive and populated than a weaker site by simple Boltzmann statistics. Those sites with very high affinity for gas molecules give rise to substantial uptake but thus contribute negatively to the desorption process. This explains why both HKUST-1 and MOF-74 performed remarkably in CH_4 uptake, but MOF-74 fared poorly in the test of usable working capacity.[38] Hence, introducing excessive unsaturated metal units that are not nodes of windows is not a good choice in practical design of MOFs with optimal methane working capacity.

3. CH_4 Redistribution upon Temperature Change in MOFs. In our computational work (Figure 4, left), the preference of adsorption sites is intensely temperature-dependent. For example, in HKUST-1, the small octahedral cages are positive to adsorption at room temperature, but do not exhibit high adsorption at low temperature (Figure 4). Therefore, it will be valuable to find the characteristic features for optimal adsorption at various environment conditions.

In the powder patterns of PCN-306 (Figure 10), (020), (021), and (202) are the main diffractions coming from the metal clusters. The intensity of the reflections (021) and (202) is decreased dramatically with decreasing temperature. In Figure 11, the weakening reflections show that additional scattering electrons were collected around the corner sites and the cage sites (Figure 2c,d), being destructive to the diffraction of metal clusters. The adsorbed CH_4 molecules at the equilibrium states were predominantly mapped in the window pockets at 295 K (Figure 11a) and around the large cage along *a*-axis at 150 K (Figure 11c). Interestingly, between the two temperatures, the CH_4 density map measured at 200 K was partially located at the window openings and partially spread around the cages (Figure 11b). As illustrated in the right-side evolution of Figure 11, the electron density maps shifted from the window pockets to the empty cages stepwise. State b is regarded as a transitional state between states a and c, redistributed among the surfaces with two types of adsorption sites.

From the neutron studies[6a,7c] and high-resolution isotherms[39] for MOF materials, it was generally thought that the low energy sites (large pores) do not start to be filled until the high energy sites (small pores) are completely occupied. However, in Figure 11b, CH_4 molecules were observed with a mixed type of adsorption sites, implying that the one-after-one filling order may be incorrect. In the enthalpic view, gas molecules should be trapped at the primary binding sites prior to the secondary sites, releasing as much adsorption heat as possible. In the entropic view, gas molecules should redistribute among several types of sites, reaching as many microstate configurations as possible. The occupation of mixed adsorption sites is an optimization between enthalpy and entropy to achieve the minimum of free energy.

In the dual-site model,[40] the heterogeneous surface was assumed to consist of two types of sites, denoted as subscripts 1

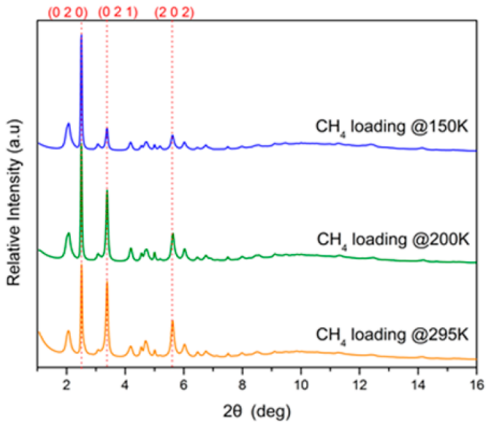

Figure 10. Powder patterns diffracted by CH_4-loaded PCN-306 at various temperatures (λ = 0.72910 Å).

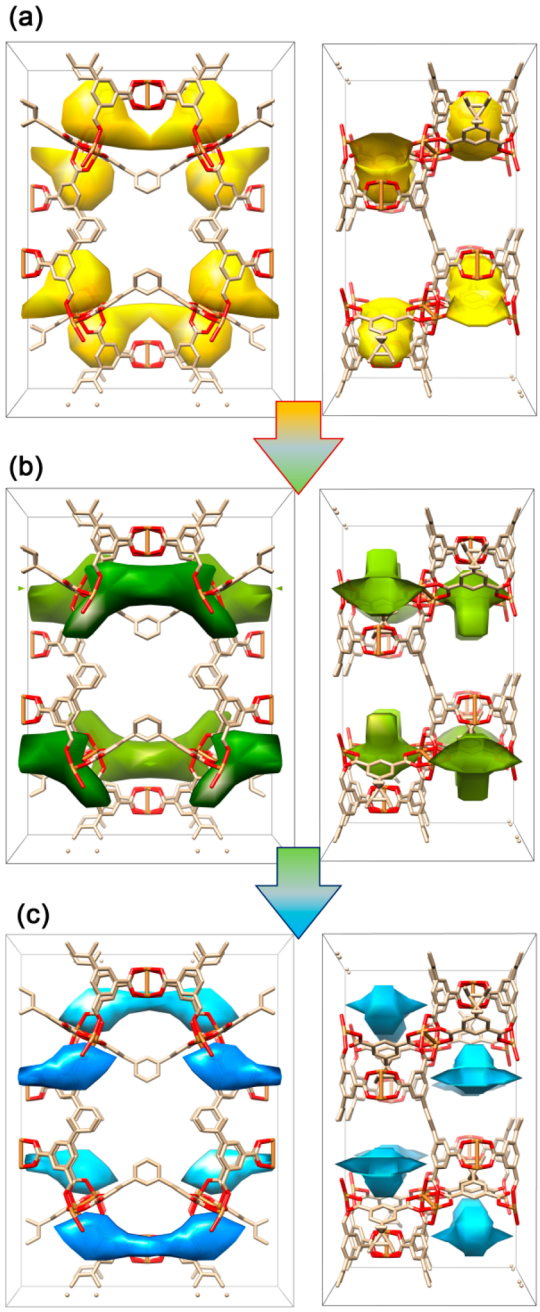

Figure 11. DED snapshots illustrate the evolution of CH_4 equilibrium states in PCN-306. The CH_4-loaded crystals were diffracted at (a) 295 K, (b) 200 K, and (c) 150 K. The right-side images, viewed along the *a*-axis, show clear different distribution around the open metal sites.

DOI: 10.1021/ja5103579
J. Am. Chem. Soc. 2015, 137, 2919−2930

and 2. The adsorption amount (v_{m1}, v_{m2}) at each site is distributively dominated by the ratio of the site fraction (f), the difference in heat of adsorption (Q_1 and Q_2), and the temperature (T). Therefore, the redistribution of gas adsorptive preference (Figure 11) can be expected under the rough condition, instead of an invariant mode:[40]

$$\frac{v_{m1}}{v_{m2}} \sim e^{(Q_2-Q_1)/RT} \quad (7)$$

if $(Q_2 - Q_1)$ is small enough with proper choice of temperature range. The temperatures between 295 and 150 K happen to be the transitional states, and the transitional states can be experimentally observed by our TRDSE work.

On the other hand, the accessibility mentioned during initial adsorption also plays an important role in this temperature-dependent evolution. It is marked that some specific positions in the structures possess molecular selectivity. In HKUST-1 (presented in Figure 4), the small octahedral cage was occupied with the molecules at 295 K but still available at lower temperatures (even contoured at zero sigma levels). The selectivity originates from the energy barrier formed by the hydrogen atoms located near the window openings. The Arrhenius equation states that higher temperature offers CH_4 molecules more energy to overcome the activation energy barrier, explaining why we only see a large number of molecules accessing the window openings at higher temperature. Using the same logic for PCN-306, it also can be seen that the window pockets are filled with CH_4 molecules at room temperature, because the energy barrier is easily overcome by the energetic molecules. Yet at lower temperatures, fewer molecules have enough kinetic energy to pass through the window openings. The above assertion can be supported by a simulation using Materials Studio,[29] which agrees that the energy barriers are hedged near the window openings (Supporting Information section 2).

Apart from being a guideline for MOF design aimed at various environments, this finding also provides a visualization of the curvature of what the Clausius−Clapeyron plot (log P vs T^{-1}) stands for. Conventionally, the total heat of adsorption (Q_{st}) has been assumed to be independent of temperature on account of the near linearity of Clausius−Clapeyron plot, suggesting an adsorption mode belonging to homogeneous surfaces. On the contrary, more instances with significant curvatures on the plot have revealed a considerable temperature coefficient of Q_{st}, which is predictively ascribed to the surface heterogeneity formed by varied energetic sites.[40]

The equilibrium state of CH_4 adsorption migrates from one type of structural feature to another upon temperature change, which implies that the heat of adsorption (Q_{ad}) in MOFs can be a function of temperature due to heterogeneous surfaces. Similar to the kinetic transition process, the thermodynamic evolution is also thought of as a molecular distribution shift, which is governed by the comprehensive concerns of both enthalpy and entropy.

4. Gas Rearrangement at Low Temperature in MOFs. It is well-known that adsorption behaviors are dependent on not only the adsorbents but the interactions of the adsorbates as well. To magnify the effect of gas−gas interactions, the PXRD data should be collected at lower temperature. No conspicuous changes arose until the temperature was lowered to 150 K.

Also, by using the DED method, we microscopically found where the CH_4 molecules were positioned. As compared to the DED map of PCN-306, it was contoured additionally near the central rhomboid space in PCN-307 where the four methyl groups build a van der Waal's force field (Figure 12b, right). As

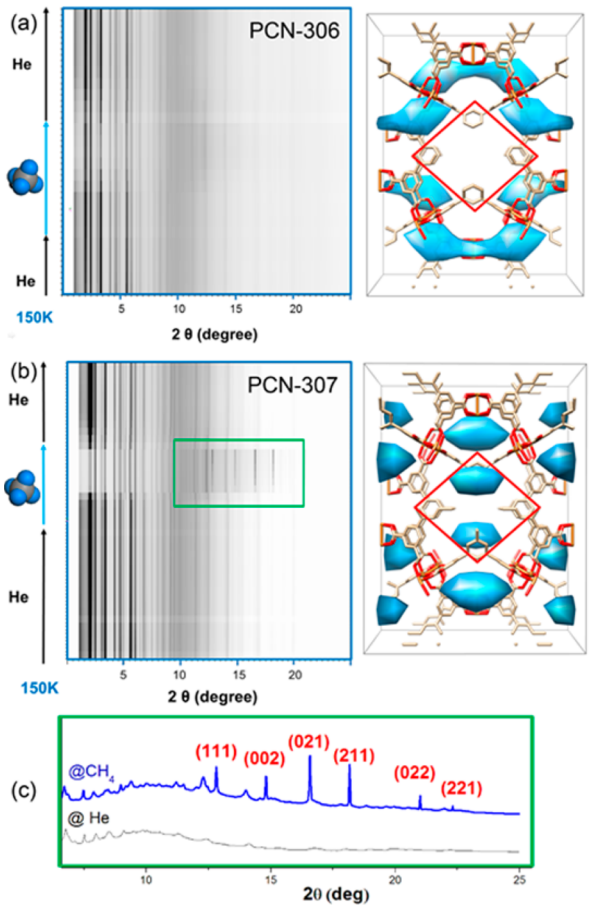

Figure 12. (Left of a,b) The top view of the in situ gas-loading-dependent PXRD patterns for PCN-306/PCN-307 at 150 K. (Right of a,b) The corresponding DED maps for CH_4 adsorption. (c) The confined methane phase grown in PCN-307 at 150 K (λ = 0.72910 Å). With the help of TOPAS 4.2, all new reflections were indexed (c) with a simple cubic unit cell with a = 5.65 Å, which is slightly shorter than a = 5.88 Å of the face-centered "phase I" reported in the methane phase diagram.[41,43]

obtained from the crystal structures, the length and the cross section of the rhomboid cavity are 5.8 Å/33.1 Å^2 for PCN-306 and 3.3 Å/20.3 Å^2 for PCN-307. It follows that at 150 K more CH_4 molecules were boxed up in PCN-307 than in PCN-306, because of the smaller rhomboid openings of PCN-307 against gas escape.

As shown in the in situ PXRD patterns (Figure 12, left), there were several nascent peaks sharply growing at the 2θ angles of 12.81°, 14.81°, 16.58°, 18.17°, 21.01°, and 22.30° in the PCN-307 diffraction image (λ = 0.72919 Å), but none presenting at the same positions in the PCN-306 pattern. Reindexing including these new peaks was done to check for phase transformation (or space group change). However, it suggested that two components coexist in the pattern. As compared to the plain pattern of PCN-306, new striking reflections were only presented in PCN-307 (Figure 12b). Attempting to find the origin of the new peaks, we found that ordered arrangement of CH_4 is the possible species simultaneously coming with the new peaks.

DOI: 10.1021/ja5103579
J. Am. Chem. Soc. 2015, 137, 2919−2930

Although we attached the new peaks to the CH_4 molecules arranged in an orderly fashion in the frameworks, CH_4 at the state of 150 K and 1 bar should be in a fluid phase[41] without new striking reflections as the plain pattern of PCN-306. The nanoscale materials should not diffract to give sharp peaks. The origin of the appearance of the new peaks is not completely explained by these hypotheses. We theorize that after achieving the critical density, pressure, and in an area of sufficient interaction with the framework, the CH_4 molecules in the largest space situate orientationally. The CH_4 molecules might be close enough to interact with each other, and thus induced to form an ordered arrangement.

If the diffractions are induced by the ordered rearrangement of methane, it might also occur during high-pressure adsorption.[42] It potentially provides some clues on how to compact more molecules in a confined space and enhance the gas uptake. This effect of functionalization in MOFs on CH_4 storage needs further investigation in the future.

Demonstration for a Practical Case: The Influence of the Methyl Groups in PCN-30X on Gas Uptake and Selectivity. PCN-306 and PCN-307 are a pair of isostructural analogues with comparable chemical composition. The only structural dissimilarity is the methyl groups located on the channels along the *c*-axis (Figure 13). According to the published results,[19] PCN-306/PCN-307 showed little difference in the CH_4 and CO_2 adsorption quantity but noteworthy contrast in CO_2/CH_4 selectivity. It was expected that the structure of PCN-307 featuring methyl groups was favored to select for CO_2 rather than similar CH_4 molecules. In this practical demonstration, the DED mapping was used to investigate this phenomenon. By comparing the DED snapshots of the two compounds (Figure 13), a rational explanation became clear.

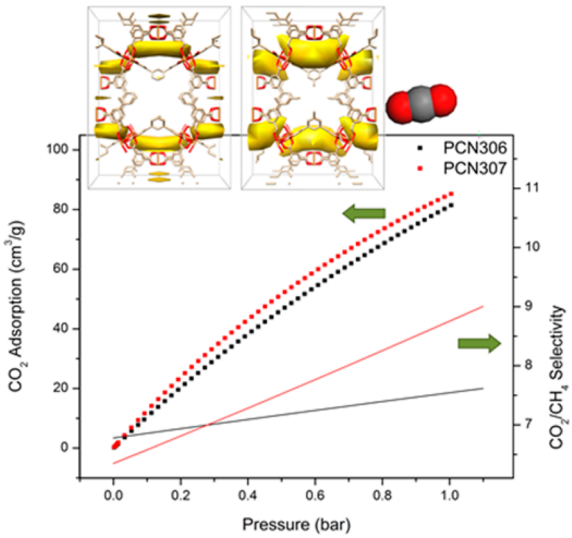

Figure 13. CO_2 sorption isotherms, the selectivity of CO_2/CH_4, and the corresponding DED maps analyzed for PCN-306/PCN-307 at 1 bar and 295 K.

The strongest contours of the CO_2 density were identified around the unsaturated metal sites in both materials, but the signals in the window pockets were detected exclusively in PCN-307. In the two structures, the entrance to the window pockets is an equilateral triangle with three 5.7 Å sides. The exit from the pockets is an isosceles triangle with the shortest sides of 5.5 Å for PCN306 and 4.7 Å for PCN-307. The smaller cross section of the exit implies that PCN-307 has a pocket with less leakage, owning a better capacity to keep smaller particles inside as well. Note that the kinetic diameter of CO_2 (3.30 Å) is smaller than that of CH_4 (3.76 Å). Additionally, the unsaturated metal sites, acting as the first agents, adsorb CO_2 molecules faster than CH_4 molecules because of CO_2's easily induced polarization. Once transferred to the window pockets of PCN-307, the CO_2 molecules seldom escape and concurrently exclude other CH_4 molecules from moving to these thermodynamically stable sites. Not instigated by the induction and attraction of methyl groups, the higher selectivity of CO_2/CH_4 in PCN-307 arises from the proper molecular access and exit constructed by the methyl groups.

CONCLUSIONS

We have demonstrated a methodology using sequential in situ powder X-ray diffraction measurements to observe dynamic sorption processes in MOFs. The mechanisms of initial adsorption, desorption, and gas redistribution on temperature change are graphically explicated by the chronological DED maps, demonstrating the power of TRDSE method. The molecular transport from one site to another is time and temperature dependent, resulting from the enthalpy-/entropy-driven redistribution among the heterogeneous surfaces to achieve the minimum of free energy. Additionally, this method demonstrated experimentally how changes in pore window size and shape both produced temperature-based pore sorption selectivity for CH_4 in HKUST-1 and explained CO_2/CH_4 selectivity changes between PCN-306 and 307.

These findings reveal the mechanisms of gas dynamics in MOFs and provide design guidance to customize MOF materials. We outlined several essentials: (i) Introducing excessive unsaturated metal units unrelated to the nodes of windows helps the adsorption kinetics upon initial gas adsorption but contributes negatively to the desorption process and overall working capacity. (ii) Both the molecular redistribution of adsorbates and the spatial accessibility of adsorbents are temperature-dependent, suggesting different positional preferences and design strategies under different temperatures. (iii) Elegant framework geometry might induce gas−gas interactions to compact more molecules, leading to higher gas uptake. (iv) Careful design of window shape and size can produce both temperature and adsorbate-dependent adsorption selectivity in particular pores in MOFs, in a predictable and now quantifiable way.

Most importantly, the TRDSE method is generally applicable to most crystalline adsorbents, yielding information on distribution ratios of adsorbates at each type of site over time, as temperature and pressure change. It provides a possible pathway to create a MOF database containing the partial adsorption enthalpy of each structural feature. We believe that prospective architectures designed for a specific need can be assembled with possible features selected in the database before hands-on experiments.

ASSOCIATED CONTENT

Supporting Information

Crystallographic data, different perspectives of the four MOF structures and the corresponding DED maps, the setup files for Superflip and Chimera programs, the GCMC simulation, and the derivation of statistical thermodynamics. This material is available free of charge via the Internet at http://pubs.acs.org.

DOI: 10.1021/ja5103579
J. Am. Chem. Soc. 2015, 137, 2919−2930

AUTHOR INFORMATION

Corresponding Author

*zhou@chem.tamu.edu

Notes

The authors declare no competing financial interest.

ACKNOWLEDGMENTS

This work was supported as part of the Methane Opportunities for Vehicular Energy (MOVE) Program under award no. DE-AR0000249 and as part of the Center for Clean-Energy-Related Gas Separation, an Energy Frontier Research Center (EFRC) funded by the U.S. Department of Energy (DOE), Office of Science, Office of Basic Energy Sciences under award no. DE-SC0001015. Y.-P.C. acknowledges EFRC (DE-SC0001015). Y.L. was supported by the Welch Foundation (A-1725). D.L. thanks the National Natural Science Foundation of China (no. 21276008) and the China Scholarship Council (CSC, no. 201208110375) for financial support. M.B. was funded by Texas A&M University. H.-C.Z. gratefully acknowledges support from the U.S. DOE (DE-AR0000073). Use of the Advanced Photon Source, an Office of Science User Facility operated for the U.S. Department of Energy (DOE) Office of Science by Argonne National Laboratory, was supported by the U.S. DOE under contract no. DE-AC02-06CH11357. Electron density graphics were performed with the UCSF Chimera package, which is developed by the Resource for Biocomputing, Visualization, and Informatics at the University of California, San Francisco (supported by NIGMS P41-GM103311). In this context, we thank Dr. Gregory J. Halder for his onsite help.

REFERENCES

(1) (a) Li, J.-R.; Ma, Y.; McCarthy, M. C.; Sculley, J.; Yu, J.; Jeong, H.-K.; Balbuena, P. B.; Zhou, H.-C. *Coord. Chem. Rev.* **2011**, *255*, 1791. (b) Makal, T. A.; Li, J. R.; Lu, W.; Zhou, H. C. *Chem. Soc. Rev.* **2012**, *41*, 7761.

(2) Zhang, M.; Bosch, M.; Gentle Iii, T.; Zhou, H.-C. *CrystEngComm* **2014**, *16*, 4069.

(3) (a) Rowsell, J. L.; Spencer, E. C.; Eckert, J.; Howard, J. A.; Yaghi, O. M. *Science* **2005**, *309*, 1350. (b) Vaidhyanathan, R.; Iremonger, S. S.; Shimizu, G. K. H.; Boyd, P. G.; Alavi, S.; Woo, T. K. *Science* **2010**, *330*, 650.

(4) (a) Zhou, C.; Cao, L.; Wei, S.; Zhang, Q.; Chen, L. *Comput. Theor. Chem.* **2011**, *976*, 153. (b) Xiang, S.; Zhou, W.; Gallegos, J. M.; Liu, Y.; Chen, B. *J. Am. Chem. Soc.* **2009**, *131*, 12415. (c) Cui, P.; Ma, Y. G.; Li, H. H.; Zhao, B.; Li, J. R.; Cheng, P.; Balbuena, P. B.; Zhou, H. C. *J. Am. Chem. Soc.* **2012**, *134*, 18892. (d) Xu, Q.; Liu, D.; Yang, Q.; Zhong, C.; Mi, J. *J. Mater. Chem.* **2010**, *20*, 706. (e) Grajciar, L. s.; Wiersum, A. D.; Llewellyn, P. L.; Chang, J.-S.; Nachtigall, P. *J. Phys. Chem. C* **2011**, *115*, 17925.

(5) (a) Wu, H.; Simmons, J. M.; Liu, Y.; Brown, C. M.; Wang, X.-S.; Ma, S.; Peterson, V. K.; Southon, P. D.; Kepert, C. J.; Zhou, H.-C.; Yildirim, T.; Zhou, W. *Chem.—Eur. J.* **2010**, *16*, 5205. (b) Duren, T.; Bae, Y. S.; Snurr, R. Q. *Chem. Soc. Rev.* **2009**, *38*, 1237. (c) Liu, D.; Zhong, C. *J. Mater. Chem.* **2010**, *20*, 10308. (d) Dubbeldam, D.; Frost, H.; Walton, K. S.; Snurr, R. Q. *Fluid Phase Equilib.* **2007**, *261*, 152.

(6) (a) Wu, H.; Zhou, W.; Yildirim, T. *J. Phys. Chem. C* **2009**, *113*, 3029. (b) Wu, H.; Zhou, W.; Yildirim, T. *J. Am. Chem. Soc.* **2009**, *131*, 4995. (c) Getzschmann, J.; Senkovska, I.; Wallacher, D.; Tovar, M.; Fairen-Jimenez, D.; Düren, T.; van Baten, J. M.; Krishna, R.; Kaskel, S. *Microporous Mesoporous Mater.* **2010**, *136*, 50. (d) Hulvey, Z.; Lawler, K. V.; Qiao, Z.; Zhou, J.; Fairen-Jimenez, D.; Snurr, R. Q.; Ushakov, S. V.; Navrotsky, A.; Brown, C. M.; Forster, P. M. *J. Phys. Chem. C* **2013**, *117*, 20116.

(7) (a) Yildirim, T.; Hartman, M. *Phys. Rev. Lett.* **2005**, *95*. (b) Wu, H.; Zhou, W.; Yildirim, T. *J. Am. Chem. Soc.* **2007**, *129*, 5314. (c) Peterson, V. K.; Liu, Y.; Brown, C. M.; Kepert, C. J. *J. Am. Chem. Soc.* **2006**, *128*, 15578. (d) Peterson, V. K.; Brown, C. M.; Liu, Y.; Kepert, C. J. *J. Phys. Chem. C* **2011**, *115*, 8851. (e) Lee, H.; Choi, Y. N.; Choi, S. B.; Seo, J. H.; Kim, J.; Cho, I. H.; Gang, S.; Jeon, C. H. *J. Phys. Chem. C* **2014**, *118*, 5691.

(8) Carrington, E. J.; Vitorica-Yrezabal, I. J.; Brammer, L. *Acta Crystallogr., Sect. B: Struct. Sci.* **2014**, *70*, 404.

(9) Yakovenko, A. A.; Wei, Z.; Wriedt, M.; Li, J.-R.; Halder, G. J.; Zhou, H.-C. *Cryst. Growth Des.* **2014**, *14*, 5397.

(10) von Schnering, H. G.; Nesper, R. *Angew. Chem., Int. Ed. Engl.* **1987**, *26*, 1059.

(11) Mackay, A. L. *Nature* **1985**, *314*, 604.

(12) Andersson, S.; Hyde, S. T.; Larsson, K.; Lidin, S. *Chem. Rev.* **1988**, *88*, 221.

(13) Brenner, S.; McCusker, L. B.; Baerlocher, C. *J. Appl. Crystallogr.* **1997**, *30*, 1167.

(14) von Schnering, H. G.; Nesper, R. *Z. Phys. B: Condens. Matter* **1991**, *83*, 407.

(15) Yakovenko, A. A.; Reibenspies, J. H.; Bhuvanesh, N.; Zhou, H.-C. *J. Appl. Crystallogr.* **2013**, *46*, 346.

(16) Serre, C.; Bourrelly, S.; Vimont, A.; Ramsahye, N. A.; Maurin, G.; Llewellyn, P. L.; Daturi, M.; Filinchuk, Y.; Leynaud, O.; Barnes, P.; Férey, G. *Adv. Mater.* **2007**, *19*, 2246.

(17) Chui, S. S. *Science* **1999**, *283*, 1148.

(18) Wang, X.-S.; Ma, S.; Forster, P. M.; Yuan, D.; Eckert, J.; López, J. J.; Murphy, B. J.; Parise, J. B.; Zhou, H.-C. *Angew. Chem., Int. Ed.* **2008**, *47*, 7263.

(19) Liu, Y.; Li, J.-R.; Verdegaal, W. M.; Liu, T.-F.; Zhou, H.-C. *Chem.—Eur. J.* **2013**, *19*, 5637.

(20) Chupas, P. J.; Chapman, K. W.; Kurtz, C.; Hanson, J. C.; Lee, P. L.; Grey, C. P. *J. Appl. Crystallogr.* **2008**, *41*, 822.

(21) Petříček, V.; Dušek, M.; Palatinus, L. *Z. Kristallogr.* **2014**, *229*, 345.

(22) There were no reflections observed in the range of 0−2°. The reflections within 16° are sufficient to describe a molecular distance of 2.6 Å, which is much shorter than the kinetic diameter of CH_4 or CO_2.

(23) Cox, D. E.; Hastings, J. B.; Thomlinson, W.; Prewitt, C. T. *Nucl. Instrum. Methods* **1983**, *208*, 573.

(24) Brenner, S.; McCusker, L. B.; Baerlocher, C. *J. Appl. Crystallogr.* **2002**, *35*, 243.

(25) Palatinus, L.; Chapuis, G. *J. Appl. Crystallogr.* **2007**, *40*, 786.

(26) (a) Pettersen, E. F.; Goddard, T. D.; Huang, C. C.; Couch, G. S.; Greenblatt, D. M.; Meng, E. C.; Ferrin, T. E. *J. Comput. Chem.* **2004**, *25*, 1605. (b) Goddard, T. D.; Huang, C. C.; Ferrin, T. E. *J. Struct. Biol.* **2007**, *157*, 281.

(27) Michalska, K. *Electron density maps and their interpretation*, 2011; http://www.man.poznan.pl/CBB/CWICZENIA/CHEM/SERP.

(28) For example, contours at a σ level of 1 would depict a closed surface, which wraps grid points possessing $\rho(x,y,z)$ values greater than one standard deviation unit above the mean. Understandably, a lower σ level would increase the volume built by the closed surface and give more noises; in contrast, a higher σ level would decrease the volume and eliminate much significant information.

(29) Accelerys. *Materials Studio Release Notes, Release 5.5.1*; Accelrys Software, Inc.: San Diego, CA, 2010.

(30) Note that the DED maps were contoured at a relative cutoff level (σ unit), not an absolute cutoff level (e/Å^3). In Figure 5, we only can say the primary adsorption sites are changed from open metal sites to window sites. Yet we cannot say the methane molecules break away from the open metal sites and transfer to the window sites. Here, we stated that the methane molecules migrate from open metal sites to windows because we confirmed the absolute cutoff level at 0.003 for Figure 5b and c and found that the volume of the electron clouds at open metal sites was indeed decreased.

(31) Lucena, S. M.; Mileo, P. G.; Silvino, P. F.; Cavalcante, C. L., Jr. *J. Am. Chem. Soc.* **2011**, *133*, 19282.

(32) George, A. R.; Catlow, C. R. A.; Thomas, J. M. *Microporous Mater.* **1997**, *11*, 97.

DOI: 10.1021/ja5103579
J. Am. Chem. Soc. 2015, 137, 2919−2930

(33) For the case of PCN-12 in Figure 6b, the gas adsorption did not reach the equilibrium. Yet for that of PCN-306, we found the electron density is almost unchanged, even as it was contoured at the absolute levels of electron density.
(34) Mason, J. A.; Veenstra, M.; Long, J. R. *Chem. Sci.* **2014**, *5*, 32.
(35) (a) Lyklema, J. *J. Chem. Soc., Faraday Trans. 2* **1977**, *73*, 1646. (b) Al-Muhtaseb, S. A.; Ritter, J. A. *J. Phys. Chem. B* **1999**, *103*, 8104. (c) Hill, T. L. *J. Chem. Phys.* **1946**, *14*, 441.
(36) Livingston, H. K. *J. Colloid Sci.* **1949**, *4*, 447.
(37) Note that CO_2 molecules can be detected at the open metal sites and small octahedral cages by contouring lower than 1 σ, which are minor adsorption sites for CO_2 adsorption.
(38) Peng, Y.; Krungleviciute, V.; Eryazici, I.; Hupp, J. T.; Farha, O. K.; Yildirim, T. *J. Am. Chem. Soc.* **2013**, *135*, 11887.
(39) (a) Krawiec, P.; Kramer, M.; Sabo, M.; Kunschke, R.; Fröde, H.; Kaskel, S. *Adv. Eng. Mater.* **2006**, *8*, 293. (b) Vishnyakov, A.; Ravikovitch, P. I.; Neimark, A. V.; Bülow, M.; Wang, Q. M. *Nano Lett.* **2003**, *3*, 713.
(40) Huang, Y.-Y. *J. Catal.* **1972**, *25*, 131.
(41) (a) Bini, R.; Pratesi, G. *Phys. Rev. B* **1997**, *55*, 14800. (b) Hazen, R. M.; Mao, H. K.; Finger, L. W.; Bell, P. M. *Appl. Phys. Lett.* **1980**, *37*, 288.
(42) Lachet, V.; Boutin, A.; Pellenq, R. J. M.; Nicholson, D.; Fuchs, A. H. *J. Phys. Chem.* **1996**, *100*, 9006.
(43) Press, W. *J. Chem. Phys.* **1972**, *56*, 2597.

DOI: 10.1021/ja5103579
J. Am. Chem. Soc. 2015, 137, 2919−2930